Measurement of cosmic-ray muon spallation products in a xenon-loaded liquid scintillator with KamLAND

```
S. Abe<sup>®</sup>, <sup>1</sup> S. Asami, <sup>1</sup> M. Eizuka, <sup>1</sup> S. Futagi, <sup>1</sup> A. Gando, <sup>1</sup> Y. Gando, <sup>1</sup> T. Gima, <sup>1</sup> A. Goto, <sup>1</sup> T. Hachiya<sup>®</sup>, <sup>1</sup> K. Hata<sup>®</sup>, <sup>1</sup>
       K. Hosokawa, <sup>1,*</sup> K. Ichimura <sup>0,1</sup> S. Ieki <sup>0,1,†</sup> H. Ikeda, <sup>1</sup> K. Inoue, <sup>1,3</sup> K. Ishidoshiro <sup>0,1</sup> Y. Kamei <sup>0,1,‡</sup> N. Kawada <sup>0,1</sup>
         Y. Kishimoto, <sup>1,3</sup> M. Koga, <sup>1,3</sup> M. Kurasawa, <sup>1</sup> T. Mitsui, <sup>1</sup> H. Miyake, <sup>1</sup> T. Nakahata, <sup>1</sup> K. Nakamura, <sup>1,§</sup> R. Nakamura, <sup>1</sup>
         H. Ozaki, <sup>1</sup> A. Sakai, <sup>1</sup> I. Shimizu, <sup>1</sup> J. Shirai, <sup>1</sup> K. Shiraishi, <sup>1</sup> A. Suzuki, <sup>1</sup> Y. Suzuki, <sup>1</sup> A. Takeuchi, <sup>1</sup> K. Tamae, <sup>1</sup>
H. Watanabe, <sup>1</sup> Y. Yoshida, <sup>1</sup> S. Obara, <sup>5,¶</sup> A. K. Ichikawa, <sup>6</sup> S. Yoshida, <sup>7</sup> S. Umehara, <sup>8</sup> K. Fushimi, <sup>9</sup> K. Kotera, <sup>10</sup> Y. Urano, <sup>10</sup> B. E. Berger, <sup>11,3</sup> B. K. Fujikawa, <sup>11,3</sup> J. G. Learned, <sup>12</sup> J. Maricic, <sup>12</sup> S. N. Axani, <sup>13</sup> Z. Fu, <sup>13</sup> J. Smolsky, <sup>13</sup> L. A. Winslow, <sup>13</sup> Y. Efremenko, <sup>14,3</sup> H. J. Karwowski, <sup>15,16</sup> D. M. Markoff, <sup>15,17</sup> W. Tornow, <sup>15,18,3</sup> S. Dell'Oro, <sup>19</sup> T. O'Donnell, <sup>19</sup> J. A. Detwiler, <sup>20,3</sup> S. Enomoto, <sup>20,3</sup> M. P. Decowski, <sup>21,3</sup> K. M. Weerman, <sup>21</sup>
                                                                      C. Grant, 22 A. Li, 22, 16 and H. Song 22
                                                                         (KamLAND-Zen Collaboration)
                                        <sup>1</sup>Research Center for Neutrino Science, Tohoku University, Sendai 980-8578, Japan
           <sup>2</sup>Department of Human Science, Obihiro University of Agriculture Veterinary Medicine, Obihiro, Hokkaido 080-8555, Japan
                     <sup>3</sup>Institute for the Physics and Mathematics of the Universe, The University of Tokyo, Kashiwa 277-8568, Japan
                                  <sup>4</sup>Graduate Program on Physics for the Universe, Tohoku University, Sendai 980-8578, Japan
                           <sup>5</sup>Frontier Research Institute for Interdisciplinary Sciences, Tohoku University, Sendai 980-8578, Japan
                                                   <sup>6</sup>Department of Physics, Tohoku University, Sendai 980-8578, Japan
                                         <sup>7</sup>Graduate School of Science, Osaka University, Toyonaka, Osaka 560-0043, Japan
                              <sup>8</sup>Research Center for Nuclear Physics (RCNP), Osaka University, Ibaraki, Osaka 567-0047, Japan
                       <sup>9</sup>Graduate School of Advanced Technology and Science, Tokushima University, Tokushima 770-8506, Japan
                           <sup>10</sup>Graduate School of Integrated Arts and Sciences, Tokushima University, Tokushima 770-8502, Japan
                           <sup>11</sup>Nuclear Science Division, Lawrence Berkeley National Laboratory, Berkeley, California 94720, USA
                          <sup>12</sup>Department of Physics and Astronomy, University of Hawaii at Manoa, Honolulu, Hawaii 96822, USA
                                          <sup>13</sup>Massachusetts Institute of Technology, Cambridge, Massachusetts 02139, USA
                             <sup>14</sup>Department of Physics and Astronomy, University of Tennessee, Knoxville, Tennessee 37996, USA
                                         <sup>15</sup>Triangle Universities Nuclear Laboratory, Durham, North Carolina 27708, USA
                                   <sup>16</sup>The University of North Carolina at Chapel Hill, Chapel Hill, North Carolina 27599, USA
                                               <sup>17</sup>North Carolina Central University, Durham, North Carolina 27701, USA
                                           <sup>18</sup>Physics Department at Duke University, Durham, North Carolina 27705, USA
                  <sup>19</sup>Center for Neutrino Physics, Virginia Polytechnic Institute and State University, Blacksburg, Virginia 24061, USA
              <sup>20</sup>Center for Experimental Nuclear Physics and Astrophysics, University of Washington, Seattle, Washington 98195, USA
                                       <sup>21</sup>Nikhef and the University of Amsterdam, Science Park, Amsterdam, the Netherlands
                                                           <sup>22</sup>Boston University, Boston, Massachusetts 02215, USA
```

(Received 23 January 2023; accepted 4 April 2023; published 22 May 2023)

Cosmic-ray muons produce various radioisotopes when passing through material. These spallation products can be backgrounds for rare event searches such as in solar neutrino, double- β decay, and dark matter search experiments. The KamLAND-Zen experiment searches for neutrinoless double- β decay in 745 kg of xenon dissolved in liquid scintillator. The experiment includes dead-time-free electronics with a high efficiency for detecting muon-induced neutrons. The production yields of different radioisotopes are measured with a combination of delayed coincidence techniques, newly developed muon reconstruction, and xenon spallation

Published by the American Physical Society under the terms of the Creative Commons Attribution 4.0 International license. Further distribution of this work must maintain attribution to the author(s) and the published article's title, journal citation, and DOI. Funded by SCOAP³.

^{*}Present address: Kamioka Observatory, Institute for Cosmic Ray Research, The University of Tokyo, Higashi-Mozumi, Kamioka, Hida, Gifu 506-1205, Japan.

[†]Corresponding author: ieki@awa.tohoku.ac.jp

^{*}Present address: RIKEN, Wako, Saitama 351-0198, Japan.

[§]Present address: Faculty of Health Sciences, Butsuryo College of Osaka, Sakai, Osaka 593-8328, Japan.

Present address: Faculty of Science, The University of Tokyo, Bunkyo-ku, Tokyo 113-0033, Japan.

[¶]Present address: National Institutes for Quantum Science and Technology, Sendai, 980-8579, Japan.

identification methods. The observed xenon spallation products are consistent with results from the FLUKA and GEANT4 simulation codes.

DOI: 10.1103/PhysRevC.107.054612

I. INTRODUCTION

Cosmic-ray muons generate radioisotopes with decay products that can be critical backgrounds for rare event experiments. Experiments searching for solar neutrinos [1,2], neutrinoless double-beta $(0\nu\beta\beta)$ decay [3,4], or dark matter interactions [5] may suffer from these backgrounds. Muons can be suppressed by locating the detector underground, for instance, the KamLAND-Zen [3,6] experiment is sited at a depth of 2700 m-water-equivalent, reducing the muon rate passing the detector to 0.34 Hz [7]. Nevertheless, the remaining muon flux can induce spallation interactions in the detector material.

The influence of spallation backgrounds can be reduced by vetoing the detector for a short time after a muon passes through, depending on the lifetimes of the produced isotopes. Since the impact on background estimates also depend on the Q values, the understanding of isotope production is crucial. Liquid scintillator (LS) or water Cherenkov detectors mainly consist of relatively light isotopes such as ¹²C and ¹⁶O, but $0\nu\beta\beta$ decay and direct detection dark matter experiments may include much heavier isotopes. Heavy isotopes can induce a larger variety of spallation products with long radioactive decay chains. Knowledge of the characteristics of the events generated by spallation processes such as the correlation of the radioisotope with the muon track and the detailed particle emission are important for background discrimination techniques. Various spallation studies have been reported from underground experiments [8–10]. One of the core challenges in this work is the efficient identification of spallation products. Muons crossing the LS leave a very large signal affecting the readout electronics and require a large dynamic range in the data acquisition system. Some spallation backgrounds, such as the small signals from capture of muon-induced neutrons after the muon passing, may be affected by these readout effects.

Cross section uncertainties impact the spallation background estimate in the energy spectrum. We compare our measurements to the energy spectra for spallation backgrounds which are reconstructed using Monte Carlo simulations (FLUKA [11,12] and GEANT4 [13–15]).

We describe the measurement of muon-induced isotopes produced in KamLAND. The data was acquired from Feb. 5th, 2019 to May 8th, 2021 and includes the $0\nu\beta\beta$ search period using 745 kg of xenon [3]. This paper is structured as follows. The experimental setup and the data acquisition system are introduced in Sec. II and the event reconstruction is reported in Sec. III. Results from FLUKA and GEANT4, the Monte Carlo (MC) programs used to simulate spallation backgrounds, are discussed in Sec. IV, followed by the spallation background measurements in Sec. V, and we summarize in Sec. VI.

II. DETECTOR

The Kamioka Liquid scintillator Anti-Neutrino Detector (KamLAND) is located about 1000 m below the peak of Mt. Ikenoyama, Gifu, Japan. The experiment contains an inner scintillation detector and an outer water Cherenkov detector (see Fig. 1). The inner detector (ID) consists of a 18 m-diameter stainless-steel spherical tank with a 13 mdiameter nylon-EVOH balloon at its center. The balloon is filled with 1 kton of LS (KamLAND-LS). The KamLAND-LS is a composition of dodecane (0.753 g/cm³), pseudocumene (0.875 g/cm³) which is also called 1,2,4-trimethylbenzene or PC, and PPO (2,5-diphyenyloxazole) as the fluor (see Table I). The density of the KamLAND-LS is 0.780 g/cm³ at 11.5°C. The remaining volume outside of the balloon is filled with nonscintillating buffer oil. The buffer oil is a mixture of 57% isoparaffin and 43% dodecane by volume. The scintillation light output is about 8000 photons/MeV, which is observed by 1325 17-inch photomultiplier tubes (PMTs) and 554 20-inch PMTs bolted to the inner surface of the stainless-steel sphere. The total photocathode coverage is 34%.

For the $0\nu\beta\beta$ decay search, a 3.8 m-diameter inner balloon (IB) [16] was installed on May 9th 2018, containing 30.5 ± 0.3 m³ of xenon-loaded LS (Xe-LS). The composition of Xe-LS is decane (0.731 g/cm³), PC (0.875 g/cm³) and PPO as shown in Table I. The KamLAND-LS is 10% brighter than Xe-LS. A total of 745 kg of xenon is dissolved in this

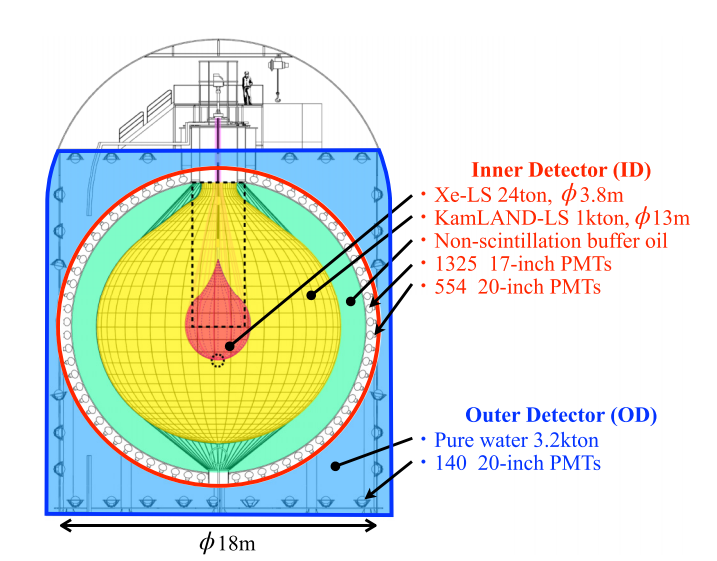


FIG. 1. Schematic view of the KamLAND-Zen detector. The black dotted rectangle, corresponding to a 1.5 m-radius cylinder in the upper hemisphere, illustrates a tube cut that is applied to exclude the droplet-like region of Xe-LS. The 0.7 m-diameter sphere centered at (x, y, z) = (0, 0, -1.9 m) is vetoed due to contamination (hot spot veto).

TABLE I. Components of the two liquid scintillators used in KamLAND-Zen.

Material	KamLAND-LS	Xe-LS
Dodecane (vol%)	80.2	_
Decane (vol%)	_	82.4
PC (vol%)	19.8	17.6
$PPO (mg/cm^3)$	1.36 ± 0.03	2.38 ± 0.02
Xe (wt%)	_	3.13 ± 0.01

scintillator. The xenon components of the Xe-LS are given in Table \overline{II} .

The outer detector (OD) is a shield for γ rays and fast neutrons from the surrounding rock. It is a 20 m-diameter and 20 m-high cylindrical cavern filled with 3.2 kton of pure water. Cosmic-ray muons are identified by detecting Cherenkov light with 20-inch PMTs, including ones with high quantum efficiency [18].

PMT waveforms are digitized by two separate data acquisition (DAQ) systems. The KamLAND Front-End Electronics (KamFEE) system has been working as the main DAQ since the beginning of KamLAND in 2002. The other system, Module for General-Use Rapid Application (MoGURA), was installed in Aug. 2010 and plays an essential role in tagging muon-induced neutrons. These neutrons are quickly thermalized with a mean capture time of 207.5 μ s, and can be identified by a 2.2 MeV capture γ ray on 1 H [7].

The KamFEE system samples PMT signals with the analog transient waveform digitizer (ATWD) from the 17-inch and 20-inch PMTs. Three amplifier gains (\times 0.5, \times 4, \times 20) cover a wide dynamic range from 1 photoelectron (p.e.) to 1000 p.e. and the waveform from each gain is digitized. An ATWD stores 128 samples with 10-bit resolution and a sampling interval of 1.5 ns. Since the analog-to-digital conversion takes 27 μs , two ATWDs are assigned to each PMT in order to avoid potential dead-time. Nevertheless, the high event rate after muon-induced events and a baseline distortion of the PMT signal introduce a significant amount of dead-time in the KamFEE electronics following muon events.

The MoGURA system was designed to be a dead-time-free DAQ system. Data are read out from 17-inch PMTs only. Unlike KamFEE, MoGURA implements a 1 GHz sampling 8-bit fast-ADC which is connected to a \times 120 gain amplifier, and three 200 MHz 8-bit sampling pipeline-ADCs each connected to separate amplifiers gains (\times 24, \times 2.4, \times 0.24). The

TABLE II. Xenon composition in the Xe-LS, based on the quality specification sheet.

	Atomic mass (u)	Volume ratio (%)	Mass (kg)
¹³⁶ Xe	135.907 [17]	90.85	677.4
¹³⁴ Xe	133.905	8.82	64.8
¹³² Xe	131.904	0.17	1.3
Others	_	0.16	1.5
Total	135.80	100.00	745.0

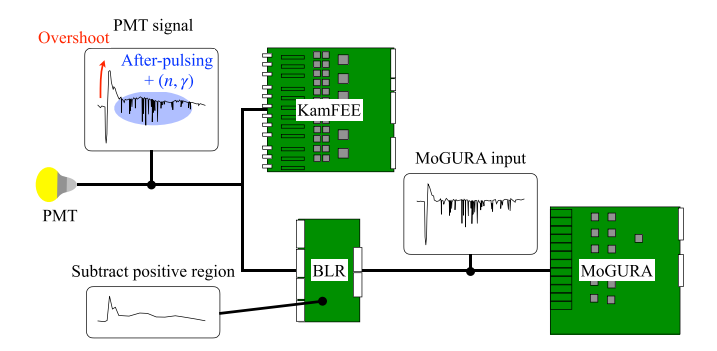


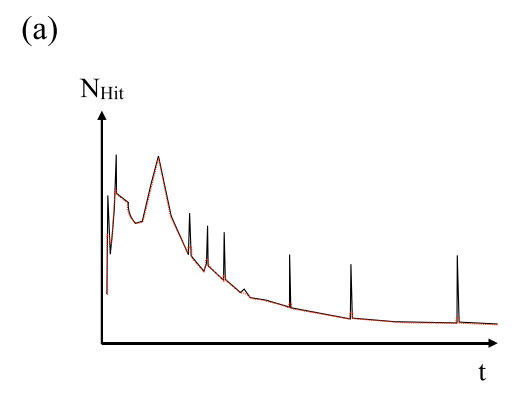
FIG. 2. Schematic of KamFEE, BLR and MoGURA. After a high charge event, the PMT baseline overshoot is subtracted and the baseline stabilized.

dynamic range of 10^5 covers from 1 p.e. to the cosmic-ray muon signal.

When high charge events occur, such as from muons, the PMT baseline is distorted for \mathcal{O} (1 ms). Small neutron capture signals follow shortly later [$<\mathcal{O}(100 \,\mu\text{s})$], so the neutron capture signals cannot be easily identified. The neutron tagging is enabled by a baseline restorer (BLR) and MoGURA's socalled adaptive mode. The BLR is an electric circuit which contributes to reducing the dead-time. The signal from each PMT is divided between a KamFEE channel and BLR (see Fig. 2). The BLR stabilizes the baseline by subtracting the overshoot region and the signal is sent to the MoGURA board. The MoGURA trigger system is continuously calculating the total number of hits (NHit) from 17-inch PMTs in a sliding time-window of 120 ns. A special trigger is launched if N_{Hit} exceeds a threshold of ≈800 and MoGURA is switched to the adaptive mode for 1 ms. In that condition, $\Delta N_{\rm Hit}$, defined as $N_{\rm Hit}$ subtracted by its 240 ns average, is calculated. Based on the $\Delta N_{\rm Hit}$ value, adaptive triggers are issued to record neutron capture events (see Fig. 3). The adaptive trigger helps discriminating signals from artifacts such as PMT afterpulsing and ringing.

III. EVENT RECONSTRUCTION

Cosmic-ray muons traversing the detector may be followed by neutron captures, β decays, and α decays of the spallation isotopes. The time-space correlations between the muons and subsequent events are key for our spallation identification techniques. Recent simulation [8] reports that the β decay isotopes are produced by muon-induced shower secondaries, rather than the cosmic-ray muons themselves, so the energy deposit of the secondaries reflect the position of spallation reactions. These aspects were taken into account by introducing track and shower position information to our delayed coincidence methods (see Sec. V). The space correlation between the β decay and neutron capture is also included in our methods. This section describes the energy calibration, cosmic-ray muon related parameters (identification, track, shower), and vertex reconstruction of neutron capture.



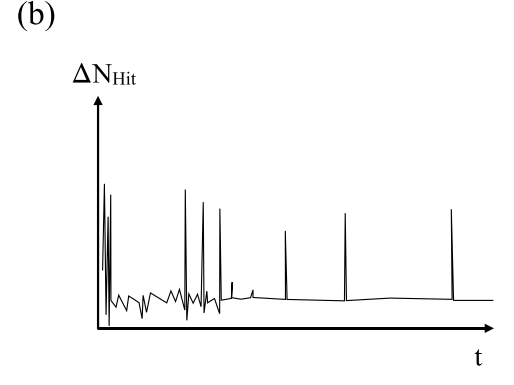


FIG. 3. Illustration of the adaptive trigger in MoGURA. (a) Number of PMT hits in a 120 ns window following a muon crossing. The red dashed line shows the average of $N_{\rm Hit}$ for 240 ns. (b) The adaptive trigger uses the difference of $N_{\rm Hit}$ and its 240-ns average to efficiently extract the sharp peaks from neutron capture events.

A. Energy calibration

The KamLAND experiment was calibrated with the radioactive sources listed in Table III. The sources were deployed at various positions within 5.5 m from the detector center by introducing an off-axis calibration system [19]. In addition, neutrons and ¹²B from spallation reactions were utilized. ¹²B ($\tau_{1/2} = 20.2$ ms, Q = 13.4 MeV) is produced uniformly in the detector and its β^- decay spectrum provides a high-energy calibration source. Neutron captures on protons produce a monochromatic γ ray at 2.2 MeV which

TABLE III. Calibration sources used in the KamLAND experiment [19].

Source	γ (MeV)
²⁰³ Hg	0.279
¹³⁷ Cs	0.662
⁶⁸ Ge	2×0.511
⁶⁵ Zn	1.116
⁶⁰ Co	1.173+1.333
241 Am $- ^{9}$ Be	2.22 ^a , (4.44, 7.65, 9.64) ^b

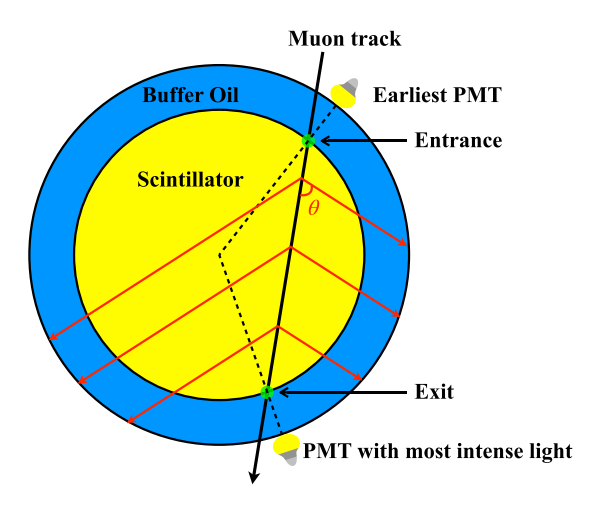


FIG. 4. Schematic of the main muon track reconstruction algorithm. The entrance point is determined by the earliest hit PMT, while the muon exit point is determined by the PMT with the largest signal. The earliest scintillation light and Cherenkov light propagate with Cherenkov angle θ .

is uniformly distributed in the LS. We correct the non-linear relation between the visible energy and the deposited energy from β rays and γ rays with a phenomenological model based on Birks quenching [20].

B. Cosmic-ray muon identification

Cosmic-ray muons are identified by measuring the large amount of scintillation and Cherenkov light associated with muons crossing the LS (LS muons). The selection criteria are defined by the total number of photoelectrons observed by the 17-inch PMTs in the ID (Q_{ID}) , where $Q_{ID} > 40000$ p.e. is an indication for a muon event.

C. Cosmic-ray muon track

A muon track is reconstructed by finding the detector entrance and exit points. The photons arriving first at the PMT determine the entrance point. For relativistic muons, both the earliest scintillation light and the Cherenkov light are emitted along the muon track with the Cherenkov angle, so that the muon exit is expected to be near the PMT which observes the most intense light. By connecting the earliest hit PMT (largest signal PMT) and the center of the detector, as shown in Fig. 4, the entrance (exit) is found at the intersection with the balloon surface. The tilt and position of the reconstructed track are corrected to minimize the deviation of the Cherenkov hit timing distribution. The algorithm can cover 97% of muons passing through the ID, but is not suitable for muon bundles, stopping muons and muons inducing energetic showers. These are identified as misreconstructed muons.

D. Muon-induced showers

Cosmic-ray muons induce particle showers by electromagnetic interactions and by hadronic interactions. Considering a shower along the muon track, the scintillation light emitted in a direction apart from the Cherenkov angle contributes to the

 $[\]frac{1}{a} {}^{1}H + n \rightarrow {}^{2}H + \gamma \text{ (2.22 MeV)}.$ ${}^{b} {}^{9}Be + \alpha \rightarrow {}^{13}C^{*} \rightarrow {}^{12}C + n + \gamma s.$

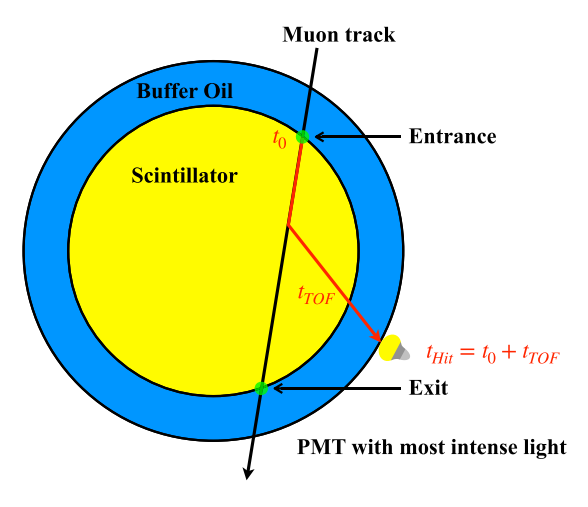


FIG. 5. Schematic of the scintillation light path of a muon event. $t_{\rm Hit}$ is the expected hit timing calculated by adding the arrival time and the time of flight.

photons which have time delays relative to the expected hits from Cherenkov angles. Assuming all photons are produced on the track, time delay can be translated to shower positions. The shower charge along the longitudinal distance is extracted from the digital waveform for each PMT. The expected hit timing ($t_{\rm Hit}$) is calculated by

$$t_{\rm Hit} = t_0 + t_{TOF},\tag{1}$$

where t_0 is the time when the muon arrives at the entrance and t_{TOF} is the time of flight for a given position on the track (see Fig. 5). $t_{\rm Hit}$ is compared with the observed waveform, and the position of photon emission is determined by minimizing the difference. Figure 6 shows an example of the reconstructed shower charge projected onto the longitudinal distance ($L_{\rm long}$) of the muon track. The peak around $L_{\rm long} \approx 1000$ cm indicates the reconstructed position of a spallation reaction.

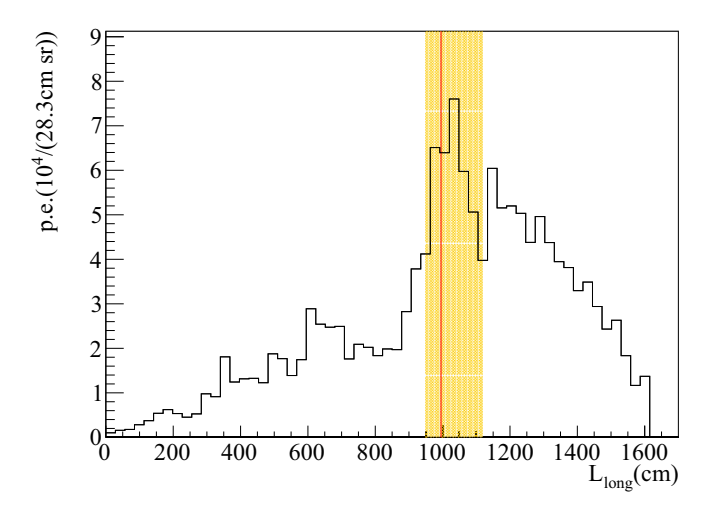


FIG. 6. An example of the reconstructed shower charge along the track of a measured muon. The red line ($L_{\rm long} = 995$ cm) is the position of the interaction. As detailed in Sec. VB, the shower charge, $dQ/dL_{\rm long} = 3.96 \times 10^5$ p.e./cm, is calculated by integrating the deposition in the orange band.

TABLE IV. Number of target nuclei (kton⁻¹) in KamLAND-LS and Xe-LS. KamLAND contains 1 kton of KamLAND-LS and 24 ton of Xe-LS.

Element	KamLAND-LS	Xe-LS
Hydrogen	8.47×10^{31}	8.39×10^{31}
Carbon	4.30×10^{31}	4.17×10^{31}
Nitrogen	5×10^{27}	8.31×10^{27}
Oxygen	5×10^{27}	8.31×10^{27}
Xenon	-	1.39×10^{29}

E. Muon-induced neutron vertex

Most of the neutrons observed in KamLAND are initiated by spallation reactions. They are immediately thermalized and captured by the components of the LS. The capture cross sections and the number of target nuclei given in Tables IV and V show that 99% of neutrons are captured by $^1\mathrm{H}$.

The capture γ -ray events are selected from the data acquired by MoGURA. The event vertex reconstruction uses a maximum likelihood estimate. We define on-time and off-time windows as follows.

(i) On-time:
$$-15 < t_i - t_{i_{TOF}} < 15 \text{ ns},$$

(ii) Off-time: $-100 < t_i - t_{i_{TOF}} < -15 \text{ ns or}$
 $15 < t_i - t_{i_{TOF}} < 100 \text{ ns},$

where $t_{i_{TOF}}$ is the time of flight between the assumed vertex and ith PMT which detected a hit at t_i . The scintillation photon hits are counted in a 200 ns time window, including multiple hits per PMT. The contribution of scintillation to the number of hits is estimated by introducing the quantity N_S which is defined as the difference of the number of on-time hits (N_{ON}) and off-time hits (N_{OFF}),

$$N_S \equiv N_{\rm ON} - N_{\rm OFF} \times \frac{30}{170}.$$
 (2)

The last factor is to compensate for the difference in time-window length. The vertex reconstruction algorithm loops over all hits. N_S is repeatedly calculated by shifting the 200 ns-time window every 20 ns. Finally, the vertex is determined for the position with maximum N_S .

Muon-induced neutron captures are extracted from N_S and the time difference to the muon (ΔT). Figure 7 shows that the neutron capture events on $^1{\rm H}$ are clustering around $N_S\approx 180$, while noise events such as after-pulsing and ringing are at $\Delta T < 30~\mu{\rm s}$. The neutron capture on $^{12}{\rm C}$ is indicated around

TABLE V. Neutron capture isotopes and their contribution to the total neutron capture in the Xe-LS [21].

Nucleus	γ (MeV)	Cross section (mb)	(%)
¹ H	2.223	332.6 ± 0.7	99.361
^{12}C	4.945	3.53 ± 0.07	0.519
¹³ C	8.174	1.37 ± 0.04	0.002
¹³⁶ Xe	4.025	238 ± 19 [22]	0.107
¹³⁴ Xe	6.36	265.1	0.011

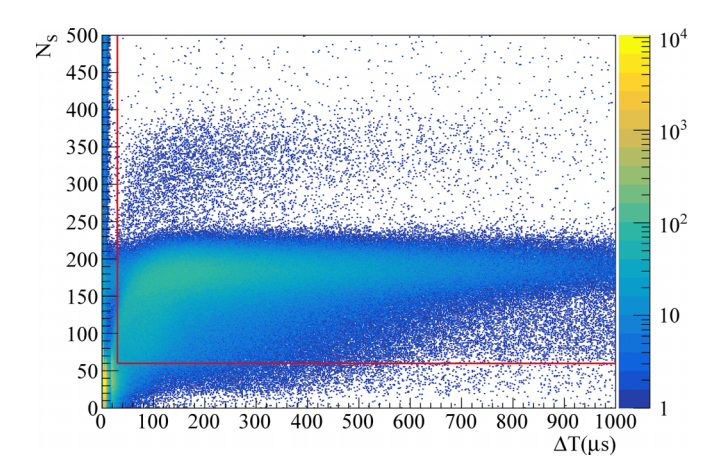


FIG. 7. N_S and ΔT distribution of neutron capture candidates in a radius less than 5.5 m. $^1{\rm H}(n,\gamma)^2{\rm H}$ events concentrate around $N_S\approx 180$. Noise events are localized around $\Delta T<30~\mu{\rm s}$. The selection criteria for neutron capture events are indicated by the red lines.

 $N_S \approx 350$ (see Fig. 8). N_S gives an estimate of the γ -ray energy.

IV. MONTE CARLO SIMULATIONS

We study spallation production with two different Monte Carlo simulation tools. The radioisotopes resulting from muon interaction with the LS are simulated with FLUKA [11,12] and subsequently their decay paths are simulated with GEANT4 [13–15]. In this section, we discuss the simulation and uncertainties of spallation isotopes in xenon with FLUKA. In addition, we discuss the reconstruction of the energy spectrum for each isotope with GEANT4.

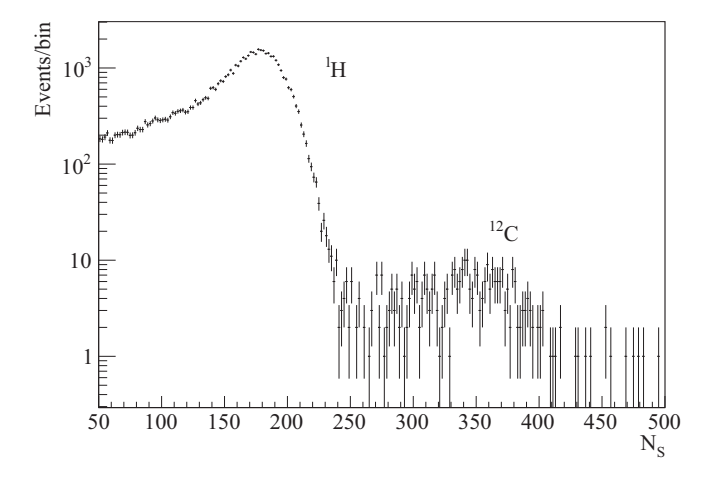


FIG. 8. N_S of the neutron capture candidates in the Xe-LS with a radius less than 1.9 m. The 2.223 (4.945) MeV γ ray from neutron capture on 1 H (12 C) gives a peak around $N_S \approx 180$ (350). The 4.025 MeV γ ray from neutron capture on 136 Xe is expected at $N_S \approx 290$ but is not visible due to background.

A. FLUKA

FLUKA is a well-studied Monte Carlo simulation tool modeling hadronic interactions. We used FLUKA 2011.08.patch to calculate the spallation production yield. The physics models that were activated for this purpose are listed in Table VI. The decay of produced radioactive nuclei and isomer production were not activated, since we traced the decay paths with GEANT4 as discussed in Sec. IV B. FLUKA was used together with the heavy ion interaction models, rQMD-2.4 [23] and DPMJET-3 [24] by linking the library.

The reproducibility of muon induced xenon spallation cross sections in FLUKA has not been tested, since there are no measurements of these cross sections yet. However, the measurement of charged hadron production with a 490 GeV positive muon beam on gaseous xenon was reported in [24]. DPMJET-3, the MC generator implemented in FLUKA, reproduced the measurement as presented in [24] demonstrating the appropriate modeling of the physics processes such as muon-nucleon scattering and hadronization processes. FLUKA is widely adopted to estimate production of particles in related fields [9,25].

To quantitatively estimate the uncertainty on production rates in FLUKA, we compared our simulation with the measurement of residual isotope production from beam experiments. Production cross sections were measured by irradiating a 1 cm³-liquid hydrogen target with a 136 Xe beam, where the incident energy per nucleon was 500 MeV [26] and 1 GeV [27]. The simulation prediction and measured cross sections are compared in Fig. 9. The deviation for the produced isotopes is large in $7 \leqslant Z \leqslant 35$ and $40 \leqslant Z \leqslant 50$, while the simulation shows good agreement in Z > 50 where the primary production yield is dominant.

The decay energy spectrum for each spallation product was determined (see Sec. IV B). The comparison between data and simulation is shown in Fig. 10 for both the 500 MeV/nucleon and 1 GeV/nucleon beams. Focusing on the region of interest (ROI) for the $0\nu\beta\beta$ decay search (2.35 $\leq E \leq$ 2.70 MeV), the result from the 500 MeV/nucleon beam shows a larger deviation, which indicates the cross section is larger for data. In the spectrum fit for the $0\nu\beta\beta$ decay search [3], the simulated shape of the xenon spallation spectrum is allowed to float within the deviation from the 500 MeV/nucleon beam measurement for a conservative approach.

The spallation product yield in the Xe-LS is calculated by emitting 2×10^7 cosmic-ray muons into a 40 m-high and 10 m-radius cylinder. The initial muon energy is generated with the MUSIC simulation framework [7,28–30]. With a detailed geometric description of Mt. Ikenoyama, MUSIC can calculate muon transportation in rock and output the survival probability. We used Gaisser's surface muon flux model [7]. The MUSIC-generated muon angular and energy spectra are sampled and act as input for the FLUKA calculation. The mean simulated muon energy is $260\pm 1\,\mathrm{GeV}$. The regions 10 m from the muon entrance and 5 m from the cylinder exit are removed from analysis in order to avoid boundary effects. The corresponding detector livetime is 9 yr as calculated from the total muon track length. The simulation with the same geometry but made of KamLAND-LS predicts the neutron

Card Physics Status PRECISIO(n) **DEFAULTS** A set of physics models PHOTONUC(lear) Gamma interactions with nuclei Activated **MUPHOTON** Muon photonuclear interaction Activated **PHYSICS** Emission of light fragments Activated by COALESCE(nse) **PHYSICS** Emission of heavy fragments Activated by EVAPORAT(ion) PHYSICS Ion electromagnetic-dissociation Activated by EM-DISSO(ciation) Deactivated by RADDECAY

Decay and isomer production

TABLE VI. FLUKA physics processes. Radioactive decay is deactivated in FLUKA since we use GEANT4 to calculate it.

capture time to be $\tau_n = 207.0 \pm 0.3 \,\mu s$ which is consistent with measurement [7]. The neutron capture rate is given in Table VII and radioisotope production is presented in Fig. 11. The simulated muon charge ratio is $\mu^+/\mu^- = 1.3$ [31].

PHYSICS

We also provide a prediction of the muon-induced spallation production yield in natural liquid xenon experiments (see Fig. 12). The simulation configuration is similar to Xe-LS, but only muons of a fixed energy are injected into a cylinder made

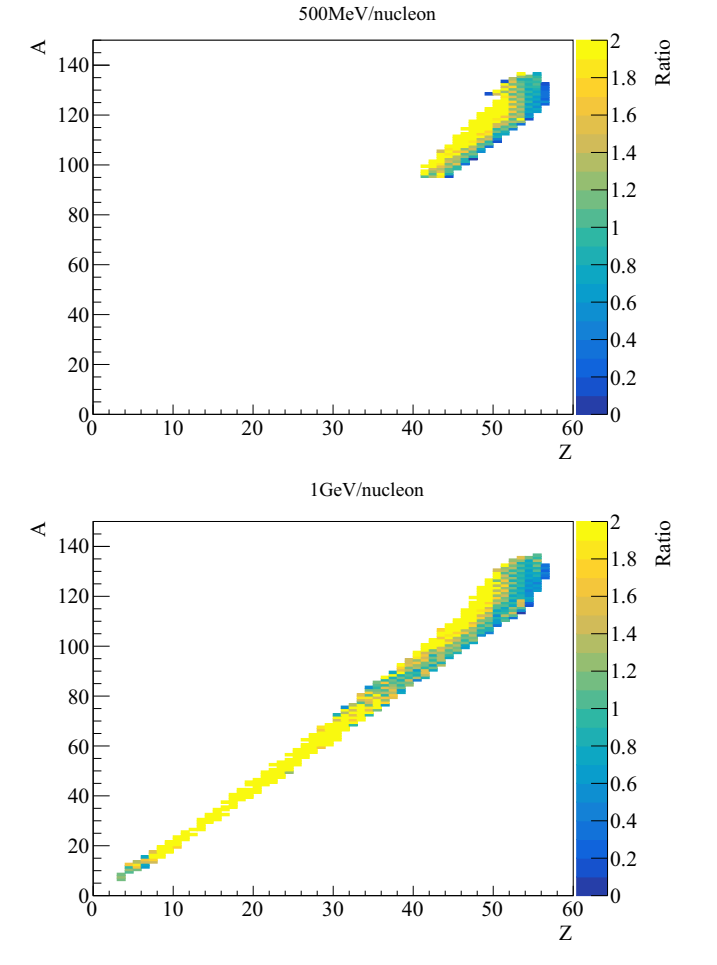


FIG. 9. The cross section ratio of the measurements to the FLUKA simulations, for a 500 MeV/nucleon ¹³⁶Xe beam (top) and a 1 GeV/nucleon 136 Xe beam (bottom). Only Z > 40 was reported in [26].

of liquid xenon. We note that FLUKA 2021.2.7 was used for the liquid xenon simulation in Fig. 12.

B. GEANT4

The xenon spallation products include long-lived isotopes. Unlike carbon, xenon can provide various unstable isotopes because of its large mass number, so sequential decays have to be taken into account for a comprehensive understanding of the backgrounds.

We use GEANT4 to estimate the radioactive decay times and to reconstruct the energy spectra. In this calculation, GEANT4 version GEANT4.10.6.p01 is used with version G4ENSDFSTATE2.2 for the Evaluated Nuclear Structure Data File (ENSDF) [21]. We confirmed the Q values, halflives, and branching ratios for more than a thousand isotopes by comparing the GEANT4 version with the online database version of ENSDF. All sequential decay products and their energy deposits were recorded and the visible energy spectrum for each isotope was simulated including the detector energy resolution and quenching effect. For each of the spallation products listed by FLUKA, 10^6 events were generated to trace the decay path. The energy spectra of some xenon isotopes are shown in Fig. 13. The simulation is executed without defining a detector geometry.

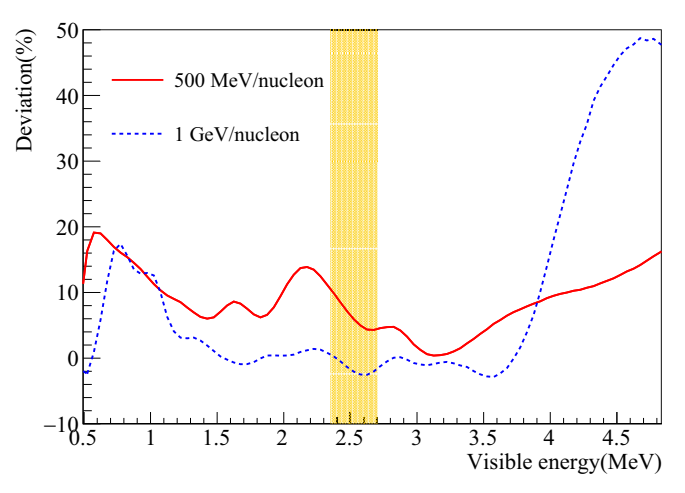


FIG. 10. Deviation of the visible spallation isotope decay energy spectrum compared to FLUKA. The data spectrum is constructed from the measured cross sections of the 500 MeV/nucleon ¹³⁶Xe beam experiment (red solid) [26] and the 1 GeV/nucleon ¹³⁶Xe beam experiment (blue dashed) [27]. The ROI is indicated by the band.

TABLE VII. Neutron capture rate in the LS with statistical uncertainty. The measured values have a 7.8 % systematic uncertainty derived from the fiducial volume, while FLUKA has a 7.2% systematic error from the estimates of \mathcal{R}_{μ} and L_{μ} .

	KamLAND-LS (kton day) ⁻¹
Data	$3781 \pm 28(\text{stat.}) \pm 295(\text{syst.})$
FLUKA	$4046 \pm 1(\text{stat.}) \pm 292(\text{syst.})$
	Xe-LS (kton day) ⁻¹
Data	$4347 \pm 98(\text{stat.}) \pm 339(\text{syst.})$
FLUKA	$4647 \pm 1(\text{stat.}) \pm 336(\text{syst.})$

V. SPALLATION PRODUCTION

This section discusses neutron capture rates and spallation productions of carbon and xenon. Since the statistics in Xe-LS is too low, the carbon spallation is estimated from KamLAND-LS data. We used FLUKA predictions for the selection efficiencies. The xenon spallation is estimated directly from the Xe-LS data, but the decomposition of individual isotopes is not possible due to the limited statistics. The uncertainties on the relative contributions are estimated based on the beam data (see Sec. IV A).

A. Neutron capture on ¹H and ¹²C

The number of neutron captures (N_n) is obtained by fitting to the data with a function of the mean capture time (τ_n) :

$$\mathcal{R}(t) = \frac{N_n}{\tau_n} e^{-(t - t_\mu)/\tau_n} + \text{const}, \tag{3}$$

where τ_n is constrained to 207.5 \pm 2.8 μ s [7] with a Gaussian penalty χ^2 term. The fit range is set to 490 \leq ΔT < 1000 μ s ($\Delta T \equiv t - t_{\mu}$) to meet the constraint and to avoid after-pulsing and PMT baseline overshoot effects. Figure 14 shows the time correlation between a cosmic-ray muon and subsequent neutron captures, where the neutron capture events are selected with 30 < ΔT < 1000 μ s and N_S > 60 in the

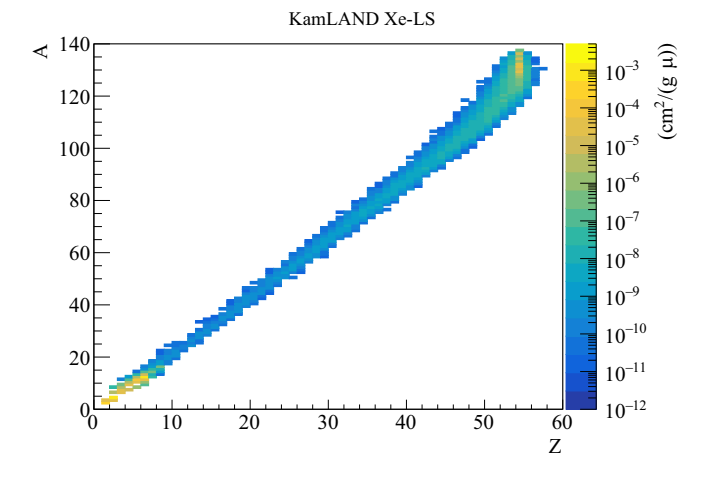
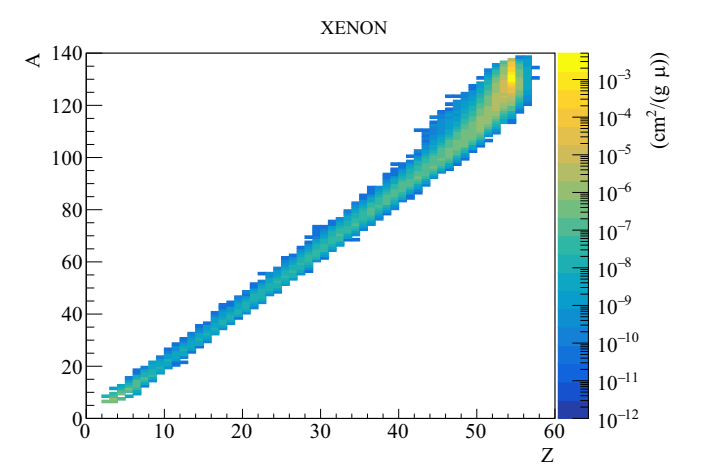


FIG. 11. Muon-induced spallation production yields in the Xe-LS from FLUKA simulation.



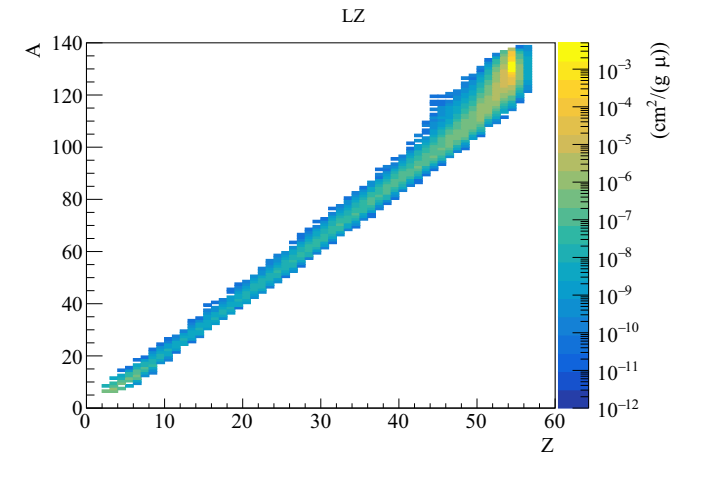


FIG. 12. Muon-induced spallation production yields in the liquid xenon from FLUKA simulations. The initial muon energy is 273 GeV and 283 GeV for XENON [32] (top) and LZ [33] (bottom), respectively. $A \leqslant 4$ is omitted.

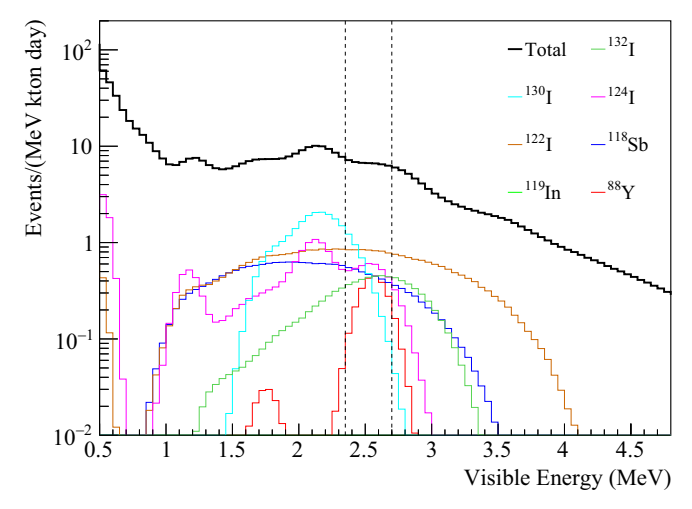


FIG. 13. Simulated visible energy spectra of spallation isotopes in Xe-LS. The colored histograms show the contribution from a part of the spallation daughters which have large impacts in the ROI. The black histogram is the total of all spallation isotopes. The $0\nu\beta\beta$ decay search ROI is indicated by black dashed lines.

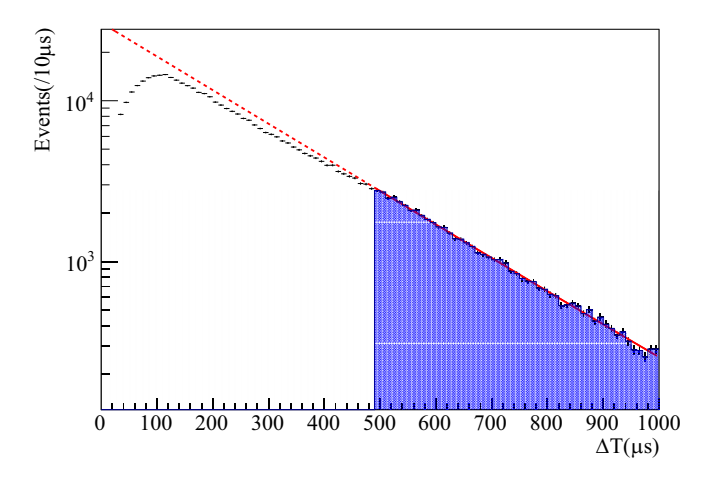


FIG. 14. Time difference between the cosmic-ray muon and neutron capture in the KamLAND-LS (2.5 < r < 4.5 m with the tube cut). The red line shows the exponential fit constrained to 207.5 \pm 2.8 μ s. Fit range is illustrated by the shaded region. The detection efficiency is lower at small ΔT due to PMT baseline overshoot.

KamLAND-LS outside of the IB (2.5 < r < 4.5 m). In addition to these selections, we apply the tube cut shown in Fig. 1. The neutron capture rate in the KamLAND-LS is found to be

$$\mathcal{R}_n = \frac{N_n}{\rho VT} = 3781 \pm 28 \text{ (kton day)}^{-1},$$
 (4)

where $\rho = 0.780 \text{ g/cm}^3$ and $V = 301.4 \text{ m}^3$ are the density and volume of the LS, respectively, and T = 711 day is the detector livetime. More generally, the neutron capture rate (and all other rates provided below) can be converted to units of cm²/(g μ), using the rate of muons passing through the KamLAND-LS, $\mathcal{R}_{\mu} = 0.198 \pm 0.014 \text{ Hz}$, and the mean track length, $L_{\mu} = 874 \pm 13 \text{ cm}$ [7],

$$\mathcal{R}_n = \frac{N_n}{\mathcal{R}_{\mu} T \rho L_{\mu}}$$
= $(2.91 \pm 0.02) \times 10^{-4} \,\text{cm}^2/(\text{g}\,\mu)$. (5)

Similarly, the neutron capture rate in the Xe-LS is obtained by selecting r < 1.9 m with the hot spot veto. The results are summarized in Table VII, together with the FLUKA predictions.

As shown in Fig. 15, the difference in capture rate between Xe-LS and KamLAND-LS appears to follow a r^3 distribution, which is in agreement with the estimation of FLUKA.

B. Carbon spallation

Cosmic-ray muons produce radioactive isotopes and neutrons in the detector. A portion of the carbon spallation backgrounds are identified by a three-fold decay coincidence (n-tag) of a LS muon (1), muon-induced neutron captures (2), and a β decay (3) with the following cuts:

- (1) $Q_{ID} > 40000$ p.e.,
- (2) $N_S > 60$ and $30 < \Delta T_{\mu-n} < 1000 \,\mu\text{s}$,
- (3) $\Delta R_{\min} < 1.6 \text{ m}.$

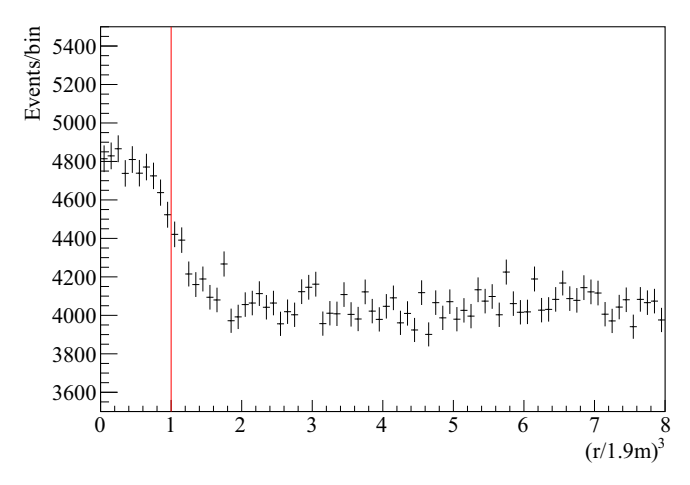


FIG. 15. Spatial distribution of neutron capture events. r is the distance from the detector center. The boundary of Xe-LS and KamLAND-LS is indicated by the red line. The vertex resolution and droplet-like shape of the inner balloon cause the deviation from a step function.

Here, $\Delta T_{\mu-n}$ is the time difference between a cosmicray muon and neutron capture, while ΔR_{\min} is the distance between the β decay and the nearest neutron capture. On the other hand, the time correlation between muon and isotope decay $(t - t_{\mu})$ is used in Eq. (6).

n-tag can discriminate neutron emitting interactions, while non-neutron emitting interactions and the β decays isolated from neutrons ($\Delta R_{\min} \ge 1.6 \text{ m}$) are covered by a shower likelihood method (shower-tag). The likelihood is constructed as a function of the reconstructed shower charge $[Q_{\text{shower}}(L_{\text{long}})]$ and transverse distance from the muon track (L_{trans}) based on the position of the isotope decay candidate events. The probability density function (PDF) of charge along the muon track $(dQ_{\text{shower}}/dL_{\text{long}})$ is provided by the shower reconstruction as described in Sec. III D. A 1.7 m window is opened around the maximum of $dQ_{\text{shower}}/dL_{\text{long}}$ and the $Q_{\text{shower}}(L_{\text{long}})$ is defined as the integral of $dQ_{\text{shower}}/dL_{\text{long}}$ in the window. The likelihood function for carbon spallation products was created based on 12 B β^- decay events, which are not selected by n-tag. ¹²B is separated by requiring a visible energy of more than 6 MeV and the time difference from a muon to be less than 150 ms. The function for accidental events is constructed assuming uniform distribution in time.

The selection efficiency of the shower likelihood method $(\epsilon_{i\text{-shower}})$ depends on the isotope, which in turn can be derived from the interaction difference of the primary particles. For example, a neutron is the most probable particle to generate ^{12}B and it prefers long L_{trans} . Pions are the leading particles in ^{10}C creation and they distribute closer to the muon track. That causes differences in the selection efficiencies between isotopes for given L_{trans} . The likelihood PDFs were created with ^{12}B events because of high statistics, but the fraction of μ^- capture process causes isotope dependence in the PDFs. To suppress the influence, we refer to the efficiency of ^8Li events obtained by (b) and (c), described later. The showertag is applied for ^{10}C , ^6He and ^{11}Be , and their efficiencies are estimated as the discrepancies from ^8Li , calculated with FLUKA.

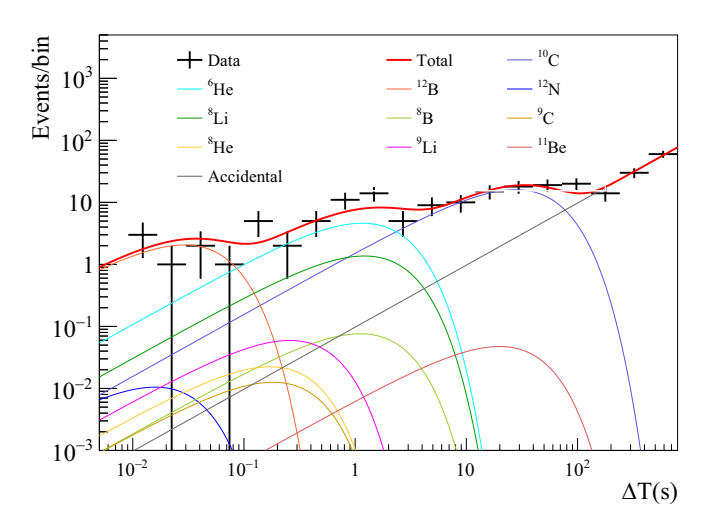


FIG. 16. Time difference between the cosmic-ray muon and the spallation isotope's β decay selected by *n*-tag. The energy bin is 2 < $E < 3 \,\mathrm{MeV}$ and the β decay candidates in 2.5 < $r < 4.0 \,\mathrm{m}$ with the tube cut are shown.

We use a binned maximum likelihood to analyze our data. It is a function of production yield of the *i*th isotope \mathcal{N}_i , lifetime τ_i , and decay energy:

$$\frac{d\mathcal{N}}{dt} = \sum_{i} \frac{\mathcal{N}_{i}}{\tau_{i}} e^{-(t-t_{\mu})/\tau_{i}} + \text{const.}$$
 (6)

The observed data are filled into log scale time bins and simultaneously fit with energy bins. Prior to this fit, the β decay candidates are categorized into three groups, in order to reduce the statistical uncertainties due to accidental background subtractions:

(a) Selected by n-tag ($\mathcal{N}_{i-n\text{-tag}}$).

- (b) Not selected by n-tag ($\mathcal{N}_{i\text{-isolated}}$).
- (c) Not selected by n-tag and selected by shower-tag

Note that (b) is the complement of (a), and (c) is a subset of (b). Equation (6) is used for each category and the production rates obtained by

(A)
$$\mathcal{N}_i = \mathcal{N}_{i-n-\text{tag}} + \mathcal{N}_{i-\text{isolated}}$$
 or

$$\begin{array}{ll} \text{(A)} \ \, \mathcal{N}_i = \mathcal{N}_{i\text{-}n\text{-}\text{tag}} + \mathcal{N}_{i\text{-}\text{isolated}} \text{ or} \\ \text{(B)} \ \, \mathcal{N}_i = \mathcal{N}_{i\text{-}n\text{-}\text{tag}} + \mathcal{N}_{i\text{-}\text{shower}} / \epsilon_{i\text{-}\text{shower}}. \end{array}$$

Background discrimination is more difficult for isotopes with a long lifetime, such as ¹⁰C, ⁶He, and ¹¹Be. That is why the production rates of those three are estimated using (B). while the others are calculated with (A). Neutron emitters (8He and 9Li) are estimated first, and short-lived isotopes (12B) and ¹²N) are second, because they have better separation. We set constraints on these four isotopes in the fit for the other isotopes.

Figure 16 shows one example of the ΔT fit result. Total production rate (kton day) $^{-1}$ of *i*th isotope is given as

$$\mathcal{R}_i = \frac{\mathcal{N}_i}{\rho V T},\tag{7}$$

where the definitions of ρ , V and T are the same as in Eq. (4). The isotope production yield in the KamLAND-LS is summarized in Table VIII. The yield in the Xe-LS is also calculated with FLUKA and the differences in carbon spallation products are a few percent, while the neutron capture rate is about 15% higher in the Xe-LS.

C. Xenon spallation

This section discusses xenon spallation with the xenon isotope composition given in Table II. ¹³⁷Xe will be addressed in Sec. VD. The spallation radioisotopes can be divided into

TABLE VIII. Summary of carbon spallation production rate and neutron capture rate in the KamLAND-LS. A unit conversion factor is provided as (kton day)⁻¹ = 7.69×10^{-8} cm²/(g μ). Spallation reactions were simulated for a KamLAND-LS cylinder and a Xe-LS cylinder, and the results are compared in the last column. For the precise estimation of ${}^{11}C$ β^+ decay, we require large statistics and the results from KamLAND is presented [34].

				Production	on rate (kton day) ⁻¹		
	$ au_{1/2}$	Q (MeV)	$\overline{\mathcal{R}_{n ext{-} ext{tag}}}$	$\mathcal{R}_{ ext{isolated}}$	$\mathcal{R}^{ ext{Data}}_{ ext{Total}}$	$\mathcal{R}_{ ext{KamLAND-LS}}^{ ext{FLUKA}}$	$\mathcal{R}_{ ext{Xe-LS}}^{ ext{FLUKA}}/\mathcal{R}_{ ext{KamLAND-LS}}^{ ext{FLUKA}}$
⁸ He	119.1 ms	10.7 (β ⁻)	$0.5^{+1.1}_{-0.5}$	$0.3^{+0.5}_{-0.3}$	$0.8^{+1.2}_{-0.5}$	0.55 ± 0.04	0.96 ± 0.03
⁹ Li	178.3 ms	13.6 (β^{-})	$2.5_{-0.3}^{+0.3}$	$0.1^{\ +0.2}_{\ -0.1}$	$2.7_{-0.4}^{+0.3}$	4.9 ± 0.4	1.00 ± 0.01
12 B	20.2 ms	13.4 (β^{-})	$43^{\ +3}_{\ -2}$	$14.4^{+0.6}_{-0.08}$	$58^{\ +3}_{\ -2}$	42 ± 3	1.013 ± 0.003
¹² N	11.0 ms	17.3 (β^+)	$0.8^{+0.9}_{-0.7}$	$0.07^{+0.2}_{-0.06}$	$0.9 ^{+0.9}_{-0.7}$	0.74 ± 0.06	1.02 ± 0.03
⁸ Li	839.9 ms	$16.0 (\beta^-)$	21^{+4}_{-3}	$0.9 {}^{+1.6}_{-0.9}$	22^{+4}_{-4}	47 ± 3	1.021 ± 0.004
^{8}B	770 ms	$18.0 (\beta^+)$	3^{+4}_{-3}	$0.8^{+1.0}_{-0.6}$	4^{+4}_{-3}	11.0 ± 0.8	1.024 ± 0.008
⁹ C	126.5 ms	$16.5 \ (\beta^+)$	1_{-1}^{+2}	$0.2^{+0.5}_{-0.2}$	2^{+2}_{-1}	1.5 ± 0.1	1.02 ± 0.02
¹¹ Be	13.8 s	11.5 (β^{-})	$1.2^{+0.3}_{-0.2}$	$0_{-0}^{+0.06}$	$1.2^{+0.3}_{-0.2}$	1.09 ± 0.08	1.02 ± 0.02
10 C	19.29 s	$3.65 (\beta^+)$	19^{+2}_{-2}	$0.5^{\ +0.6}_{\ -0.5}$	19^{+2}_{-2}	23 ± 2	1.029 ± 0.005
⁶ He	806.7 ms	$3.51~(\beta^{-})$	10^{+1}_{-1}	$1 {}^{+1}_{-1}$	11^{+2}_{-1}	28 ± 2	1.022 ± 0.005
11 C	1221.8 s	1.98 (β^{+})	_	_	$973 \pm 10 [34]$	679 ± 49	1.012 ± 0.001
n	207.5 μs	$2.223(\text{cap.}\gamma)$	_	_	3781 ± 296	4046 ± 292	1.1485 ± 0.0004

TABLE IX. Simulated production rate of dominant isotopes in $2.35 \leqslant E \leqslant 2.70$ MeV in Xe-LS.

		(kton day) ⁻¹		
	$\tau_{1/2}$ (s)	Q (MeV)	ROI	Total
⁸⁸ Y	9.212×10^{6}	$3.62 \left(EC/\beta^+ \gamma \right)$	0.110	0.136
90m1 Zr	8.092×10^{-1}	2.31 (IT)	0.012	0.093
⁹⁰ Nb	5.256×10^4	6.11 (EC/ $\beta^{+}\gamma$)	0.024	0.095
⁹⁶ Tc	3.698×10^{5}	$2.97 (EC/\beta^+\gamma)$	0.012	0.059
98Rh	5.232×10^{2}	$5.06 (EC/\beta^+ \gamma)$	0.011	0.076
¹⁰⁰ Rh	7.488×10^4	$3.63 \left(EC/\beta^+ \gamma \right)$	0.088	0.234
¹⁰⁴ Ag	4.152×10^3	$4.28 (EC/\beta^+\gamma)$	0.012	0.160
104m1 Ag	2.010×10^3	$4.28 \left(\text{EC}/\beta^+ \gamma \right)$	0.018	0.111
¹⁰⁷ In	1.944×10^{3}	$3.43 (EC/\beta^+\gamma)$	0.019	0.135
¹⁰⁸ In	3.480×10^{3}	$5.16 \left(EC/\beta^+ \gamma \right)$	0.089	0.194
¹¹⁰ In	1.771×10^4	$3.89 \left(EC/\beta^+ \gamma \right)$	0.053	0.236
110m1 In	4.146×10^{3}	$3.89 \left(EC/\beta^+ \gamma \right)$	0.066	0.351
¹⁰⁹ Sn	1.080×10^{3}	$3.85 \left(EC/\beta^+ \gamma \right)$	0.027	0.122
¹¹³ Sb	4.002×10^{2}	$3.92 \left(EC/\beta^+ \gamma \right)$	0.036	0.231
¹¹⁴ Sb	2.094×10^{2}	$5.88 \left(EC/\beta^+ \gamma \right)$	0.020	0.297
¹¹⁵ Sb	1.926×10^{3}	$3.03 \left(EC/\beta^+ \gamma \right)$	0.031	0.839
¹¹⁶ Sb	9.480×10^{2}	4.71 (EC/ $\beta^{+}\gamma$)	0.071	0.939
¹¹⁸ Sb	2.160×10^{2}	$3.66 \left(EC/\beta^+ \gamma \right)$	0.165	1.288
¹²⁴ Sb	5.201×10^6	$2.90 (EC/\beta^-\gamma)$	0.016	0.054
¹¹⁵ Te	3.480×10^{2}	$4.64 \left(EC/\beta^+ \gamma \right)$	0.012	0.124
¹¹⁷ Te	3.720×10^3	$3.54 \left(EC/\beta^+ \gamma \right)$	0.052	0.594
^{119}I	1.146×10^{3}	$3.51 \left(EC/\beta^+ \gamma \right)$	0.053	0.533
^{120}I	4.896×10^{3}	$5.62 \left(EC/\beta^+ \gamma \right)$	0.091	0.953
^{122}I	2.178×10^{2}	$4.23 \left(EC/\beta^+ \gamma \right)$	0.289	1.965
^{124}I	3.608×10^{5}	$3.16 \left(EC/\beta^+ \gamma \right)$	0.190	1.654
^{130}I	4.450×10^4	$2.95 (\beta^- \gamma)$	0.195	1.188
^{132}I	8.262×10^{3}	$3.58 (\beta^- \gamma)$	0.148	0.427
^{134}I	3.150×10^3	$4.18 (\beta^- \gamma)$	0.043	0.183
¹²¹ Xe	2.406×10^{3}	$3.75 \left(EC/\beta^+ \gamma \right)$	0.100	0.540
¹²⁵ Cs	2.802×10^{3}	$3.09 \left(EC/\beta^+ \gamma \right)$	0.012	0.266
¹²⁶ Cs	9.840×10^{1}	$4.82 \left(EC/\beta^+ \gamma \right)$	0.011	0.080
¹²⁸ Cs	2.196×10^{2}	$3.93 \left(EC/\beta^+ \gamma \right)$	0.031	0.229

two categories: isotopes directly created by spallation and their daughter isotopes. The former is given by the FLUKA simulation and GEANT4 is used for the latter. We assume that the abundance of daughter nuclei are in equilibrium, so that the production yield of the *n*th daughter particle in a decay chain is given by

$$\mathcal{N}_n(t, \mathcal{N}_0, r) = \frac{r}{\lambda_n} + \frac{1}{\lambda_n} \sum_{i=1}^n \left(\mathcal{N}_0 - \frac{r}{\lambda_i} \right) \prod_{j \neq i}^n \left(\frac{\lambda_j}{\lambda_j - \lambda_i} \right) e^{-\lambda_i t}.$$
(8)

 \mathcal{N}_0 is the initial abundance of the parent isotope, r is the continuous production rate of the parent, and λ_n is the decay constant for the nth isotope. Production yields of daughters are calculated using RadioactiveDecay in GEANT4. The

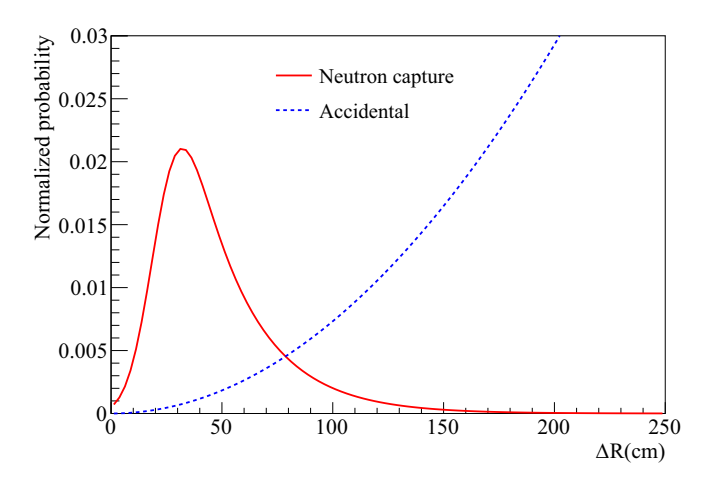


FIG. 17. PDFs of neutron capture events and accidental coincidences in Eq. (10) are given as red solid line and blue dashed line, respectively.

equilibrium of a parent isotope can be approximated as a 2000 days exposure of cosmic-ray muons to Xe-LS.

The dominant backgrounds due to xenon spallation in the ROI are enumerated in Table IX. Many isotopes have lifetimes of a few days or longer. A simple delayed coincidence method for rejection is therefore not practical considering the detector livetime.

Most of the listed isotopes are directly produced by spallation reactions. A lager mass difference between ¹³⁶Xe and the daughter particle is an indication of a greater amount of neutron emission in the xenon spallation reaction. That is the reason we introduced neutron multiplicity into our xenon spallation identification.

The xenon spallation events are selected by a cut to the likelihood ratio,

$$\mathcal{LR} = \frac{\mathcal{L}_{xe}}{\mathcal{L}_{xe} + \mathcal{L}_{acc}},\tag{9}$$

where $\mathcal{L}_{xe}(\mathcal{L}_{acc})$ is a likelihood of the xenon spallation (accidentals) constructed as a function of ΔT , ΔR_{min} , and the effective number of neutron captures $(N_{n_{eff}})$. ΔT and ΔR_{min} are introduced in Secs. V A and V B, while $N_{n_{eff}}$ is defined as follows:

$$N_{n_{\text{eff}}} \equiv \sum_{j} \frac{P_{n}(\Delta R_{j})}{P_{n}(\Delta R_{j}) + P_{\text{acc}}(\Delta R_{j})},$$
 (10)

where ΔR_j is the distance between a β decay and the *j*th neutron capture, P_n and $P_{\rm acc}$ are PDFs of neutron capture events and accidental coincidences (see Figs. 17, 18).

 \mathcal{L}_{xe} is calculated by iterating over the *i*th daughter nucleus:

$$\mathcal{L}_{xe} = \sum_{i} P_{xe_i}(\Delta R_{\min}, N_{n_{\text{eff}}}, \Delta T), \tag{11}$$

$$\mathcal{L}_{\text{acc}} = P_{\text{acc}}(\Delta R_{\text{min}}, N_{n_{\text{eff}}}, \Delta T), \tag{12}$$

where the likelihood PDFs of xenon spallation (P_{xe_i}) are made assuming the production ratio of daughters follow the FLUKA prediction, while accidental PDFs (P_{acc}) to be uniform in time and space. Selected events with $\Delta T < 4 \times 10^5$ s are vetoed,

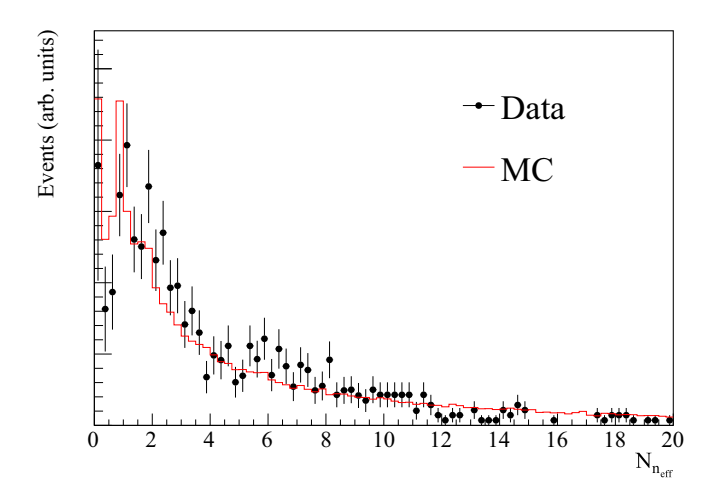


FIG. 18. Neutron multiplicity of ¹⁰C from simulation (red line) and data (black points) in r < 4 m with the tube cut and the hot spot veto.

 \approx 9% of dead-time. The choice of the veto time is based on the trade off between veto efficiency and dead-time. The selection efficiency is evaluated to be $42.0 \pm 8.8 \%$.

In the $0\nu\beta\beta$ decay search, we estimate the $0\nu\beta\beta$ decay rate and xenon spallation rate by the fit to the energy spectrum. The background models and vetoes are detailed in [3]. After applying the vetoes and the xenon spallation likelihood selection to the $0\nu\beta\beta$ decay candidates, the xenon spallation production rate is evaluated from a Poisson- χ^2 scan as shown in Fig. 19. We observe a xenon spallation rate of 3.5 \pm 0.6 (kton day)⁻¹ in $2.35 \leqslant E \leqslant 2.70$ MeV, while the simulation prediction is $2.6 \pm 0.2 \, (\text{kton day})^{-1}$.

The time difference between the cosmic-ray muon and xenon spallation candidates provides another estimate for the xenon spallation production (Fig. 20). Xenon spallation candidates in 2.4 < E < 3.0 MeV and r < 1.6 m with the hot

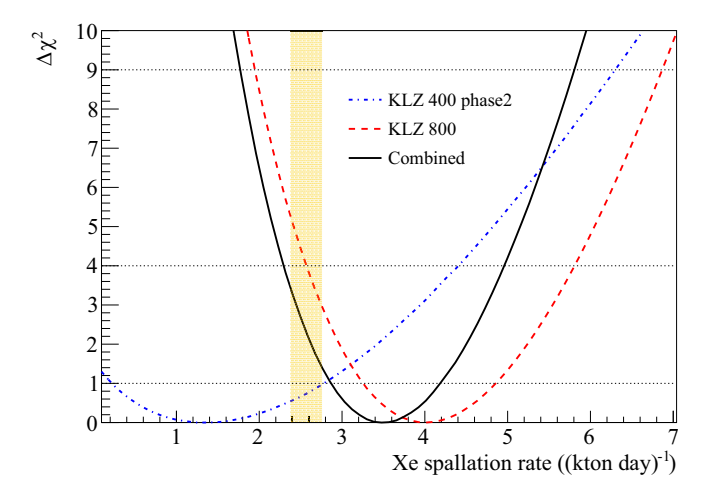


FIG. 19. $\Delta \chi^2$ of the xenon spallation rate fitted to the energy spectrum. The results of KamLAND-Zen 400 phase2 and KamLAND-Zen 800 are shown as blue and red dashed lines, and the combined result is shown in black. The FLUKA prediction is indicated with an orange band.

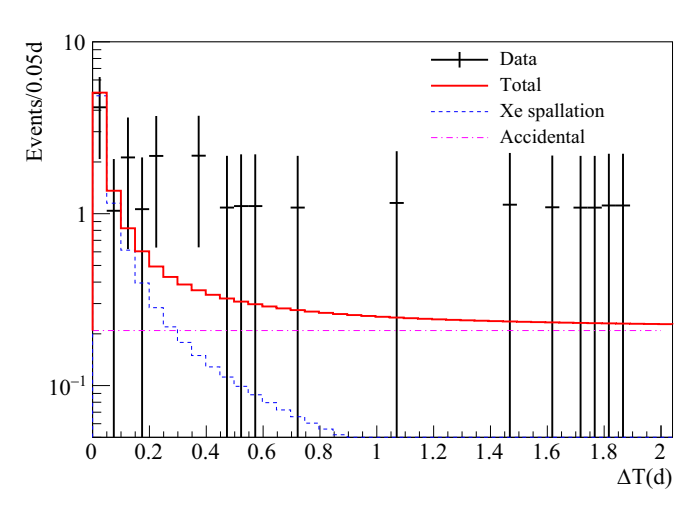


FIG. 20. Time difference between the cosmic-ray muon and xenon spallation candidates. The data was plotted after correcting the muon detection efficiency.

spot veto are selected, where the detector livetime is 625 days and Xe-LS mass 13 ton. In order to discriminate the spallation events other than xenon spallation, (a) a 150-ms-veto, (b) a 180-s-veto, and (c) a 27-min-veto were applied after the muon, where (b) and (c) require three-fold tagged events. Short lifetime spallation events are removed by (a). 10 C β^+ decay is discriminated by (b) and 137 Xe β^- decay is suppressed using (c) in combination with the requirement of more than one emitted neutron with $N_S > 240$.

Accidental coincidences are discriminated by requiring $N_{n_{\rm off}} \geqslant 6$. We assume that accidental coincidences follow a Poisson distribution with an average event rate of 3.6 /day. The number of observed events in $0 < \Delta T < 1$ day is 16, which deviates from the accidental only model by 4.8 σ . Poisson- χ^2 is calculated as a function of the production ratio of measurement to simulation. The ratio was estimated at $1.27^{\,+\,0.47}_{\,-0.4}$.

D. Neutron capture on ¹³⁶Xe

The neutron capture reaction on \$^{136}\$Xe is followed by 137 Xe β^- decay ($\tau_{1/2} = 3.8 \text{ min}, Q = 4.173 \text{ MeV}$):

(1)
136
Xe + $n \rightarrow ^{137}$ Xe + γ ,
(2) 137 Xe $\rightarrow ^{137}$ Cs + $\beta^- + \bar{\nu_e} + \gamma$.

(2)
137
Xe $\rightarrow ^{137}$ Cs $+\beta^- + \bar{\nu_e} + \gamma$.

Using the neutron capture ratio of ¹³⁶Xe, according to Table V, and the measured neutron capture rate in the Xe-LS, see Table VII, the event rate of neutron capture on ¹³⁶Xe is expected to be

$$\mathcal{R}_{^{137}\text{Xe}} = 4347 \times 0.00107$$

= $4.6 \pm 0.5 \, (\text{kton day})^{-1}$, (13)

while the FLUKA prediction is 5.5 ± 0.4 (kton day)⁻¹.

We identify 137 Xe β^- decay by a triple coincidence of a LS muon, the γ ray from neutron capture ($E_{\gamma} = 4.025 \,\text{MeV}$) and the subsequent β^- decay. The γ ray and the β^- decay are selected by a likelihood

$$\mathcal{L} = \max(P(\Delta R) \cdot P(N_S)) \cdot P(N_{n_{\text{eff}}}), \tag{14}$$

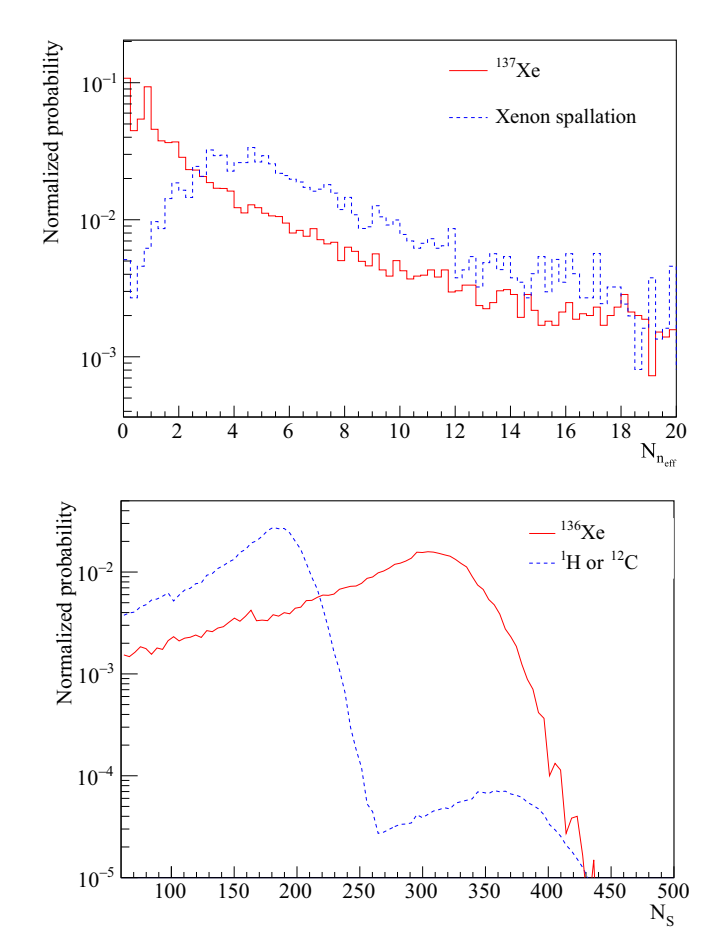


FIG. 21. Upper figure shows the PDFs of neutron multiplicity of 137 Xe events (red solid line) and other xenon spallation events (blue dashed line). Bottom figure shows the PDFs of N_S for neutron captures on 136 Xe (red solid line) and 1 H and 12 C (blue dashed line).

where ΔR , N_S , and $N_{n_{\text{eff}}}$ are defined in previous sections and the PDFs are given in Figs. 17 and 21. $P(\Delta R) \cdot P(N_S)$ is calculated for each neutron capture and search for a neutron close to the β decay with high N_S .

The dominant backgrounds for the measurement of neutron capture on $^{136}\mathrm{Xe}$ are carbon and xenon spallation, two-neutrino double- β decay and radioactive impurities. The $^{11}\mathrm{C}$ β^+ decay and two-neutrino double- β decay rates are negligible in 2.4 \leqslant E < 3.2 MeV, while $^{12}\mathrm{B}$ β^- decay is rejected by a 150 ms-veto after a cosmic-ray muon. Other carbon spallation backgrounds, with $^{10}\mathrm{C}$ β^+ decay the most critical, are suppressed by vetoing the events which are selected by n-tag in Sec. VB and observed within 80 s from the cosmic-ray muon. The xenon spallation backgrounds and radioactive impurities are suppressed by a cut to the likelihood ratio.

Similar to the measurement of carbon spallation production in Eq. (6), the capture rate is obtained from a simultaneous fit to time and energy. Figure 22 shows the time difference between a cosmic-ray muon and the 137 Xe β^- decay candidate which is located within 1.9 m from the detector center. The detector livetime is 646 d and the Xe-LS mass is 22 ton. The visible energy spectrum of the 137 Xe β^- decay candidates

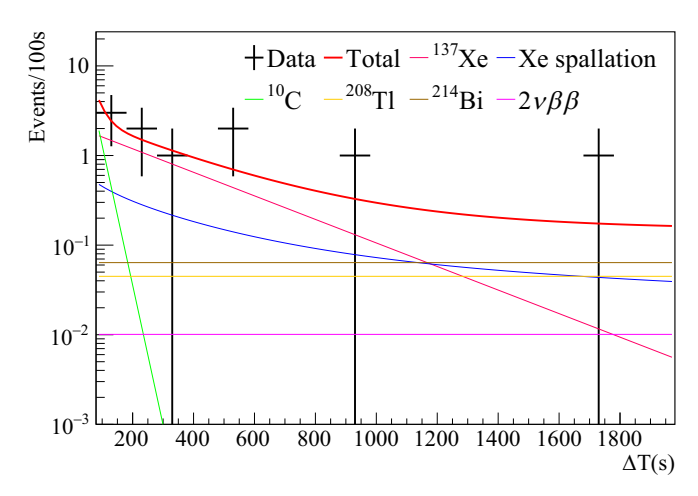


FIG. 22. Time difference between a cosmic-ray muon and the 137 Xe β^- decay candidate in 2.4 $\leqslant E < 3.2$ MeV. 208 Tl β^- decay is derived from the 232 Th series.

in $80 \le \Delta T < 1980$ s is shown in Fig. 23. The event rate of ^{10}C β^+ decay and xenon spallation are constraint from the measurements in Secs. VB and VC. The number of events is evaluated from a Poisson- χ^2 scan. We observe 4.6 \pm 2.8 (stat.) \pm 0.2 (syst.) (kton day) $^{-1}$ of neutron captures on ^{136}Xe , corresponding to 236 \pm 145 mb. The measurement is consistent with the expectation in Eq. (13) using the ^{136}Xe capture cross section of [22].

VI. SUMMARY

The radioisotopes production caused by cosmic-ray muon spallation in a xenon-loaded liquid scintillator was measured with KamLAND and compared to results from the FLUKA and GEANT4 simulation codes. The production yield of carbon spallation isotopes is consistent with our previous measurement [7] and additionally the ⁶He production rate is measured for the first time. These measurements were done using a combination of delayed coincidence with a higher neutron detection efficiency and the shower likelihood

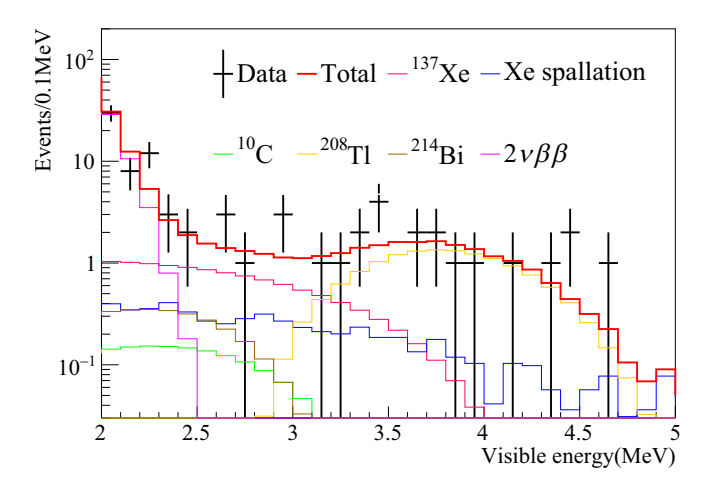


FIG. 23. Visible energy of the $^{137}{\rm Xe}~\beta^-$ decay candidates in $80\leqslant \Delta T<1980~{\rm s}.$

method to cover the contribution from non-neutron emitting reactions.

The xenon spallation productions including their subsequent decays were studied with FLUKA and GEANT4 simulations. Figure 13 and Table IX show the non-negligible isotopes for the $0\nu\beta\beta$ decay search. Their contributions in the ROI is estimated to be 2.6 ± 0.2 (kton day)⁻¹.

We developed a likelihood method which effectively utilizes the space correlation of muon-induced neutron captures and their multiplicity, resulting in a xenon spallation selection efficiency of $42.0 \pm 8.8 \,\%$. The observed amount of xenon spallation production is $3.5 \pm 0.6 \,(\text{kton day})^{-1}$ in $2.35 \leqslant E \leqslant 2.70 \,\text{MeV}$, an important background for the $0\nu\beta\beta$ decay search. One of the possible approaches to refine the background discrimination is through particle identification, since most of the xenon spallation decays are accompanied by γ rays.

The 137 Xe β^- decay is an inevitable background for the $0\nu\beta\beta$ search with 136 Xe. We measured the production yield using a two-dimensional binned likelihood fit. Although there are large statistical uncertainties, a significant amount of neutron capture on 136 Xe is observed. The observation is consistent with the expectation from [22].

ACKNOWLEDGMENTS

The KamLAND-Zen experiment is supported by JSPS KAKENHI Grants No. 21000001, No. 26104002, and No. 19H05803; the Dutch Research Council (NWO); and under the US Department of Energy (DOE) Grant No. De-AC02-05CH11231, other DOE, and NSF grants to individual institutions. We appreciate the supports of the Kamioka Mining and Smelting Company for activities in the mine, and NII for SINET4 as well.

- [1] K. Abe *et al.* (Super-Kamiokande Collaboration), Phys. Rev. D 94, 052010 (2016).
- [2] B. Aharmim *et al.* (SNO Collaboration), Phys. Rev. C 88, 025501 (2013).
- [3] S. Abe *et al.* (KamLAND-Zen Collaboration), Phys. Rev. Lett. **130**, 051801 (2023).
- [4] G. Anton *et al.* (EXO-200 Collaboration), Phys. Rev. Lett. **123**, 161802 (2019).
- [5] E. Aprile *et al.* (XENON Collaboration), Phys. Rev. D 102, 072004 (2020).
- [6] A. Gando, Y. Gando, T. Hachiya, A. Hayashi, S. Hayashida, H. Ikeda *et al.* (KamLAND Collaboration), Phys. Rev. Lett. 117, 082503 (2016).
- [7] S. Abe *et al.* (KamLAND Collaboration), Phys. Rev. C 81, 025807 (2010).
- [8] S. W. Li and J. F. Beacom, Phys. Rev. D 91, 105005 (2015).
- [9] G. Bellini et al., J. Cosmol. Astropart. Phys. 08 (2013) 049.
- [10] A. Li et al., Phys. Rev. C 107, 014323 (2023).
- [11] T. T. Böhlen et al., Nucl. Data Sheets 120, 211 (2014).
- [12] A. Ferrari, P. R. Sala, A. Fasso, and J. Ranft, CERN-2005-10, INFN/TC_05/11, SLAC-R-773 (2005).
- [13] S. Agostinelli *et al.*, Nucl. Instrum. Methods Phys. Res. A **506**, 250 (2003).
- [14] J. Allison et al., IEEE Trans. Nucl. Sci. 53, 270 (2006).
- [15] J. Allison *et al.*, Nucl. Instrum. Methods Phys. Res. A **835**, 186 (2016).
- [16] Y. Gando et al. (KamLAND collaboration), J. Inst. 16, P08023 (2021).
- [17] M. Redshaw, E. Wingfield, J. McDaniel, E. G. Myers et al., Phys. Rev. Lett. 98, 053003 (2007).
- [18] H. Ozaki, J. Shirai et al. (KamLAND Collaboration), PoS (ICHEP 2016), 1161 (2016).

- [19] B. E. Berger et al., J. Inst. 4, P04017 (2009).
- [20] J. B. Birks, Proc. Phys. Soc. A 64, 874 (1951).
- [21] National Nuclear Data Center, Brookhaven National laboratory, Evaluated Nuclear Structure Data File, https://www.nndc.bnl. gov.
- [22] J. B. Albert, S. J. Daugherty, T. N. Johnson, T. O'Conner, L. J. Kaufman, A. Couture, J. L. Ullmann, and M. Krticka, Phys. Rev. C 94, 034617 (2016).
- [23] H. Sorge, H. Stoecker, and W. Greiner, Ann. Phys. 192, 266 (1989).
- [24] M. R. Adams *et al.* (E665 Collaboration), Z. Phys. C **61**, 179 (1994).
- [25] J. B. Albert et al., J. Cosmol. Astropart. Phys. 04 (2016) 029.
- [26] L. Giot et al., Nucl. Phys. A 899, 116 (2013).
- [27] P. Napolitani, K.-H. Schmidt, L. Tassan-Got, P. Armbruster, T. Enqvist, A. Heinz, V. Henzl, D. Henzlova, A. Kelić, R. Pleskač, M. V. Ricciardi, C. Schmitt, O. Yordanov, L. Audouin, M. Bernas, A. Lafriaskh, F. Rejmund, C. Stéphan, J. Benlliure, E. Casarejos, M. Fernandez Ordonez, J. Pereira, A. Boudard, B. Fernandez, S. Leray, C. Villagrasa, and C. Volant, Phys. Rev. C 76, 064609 (2007).
- [28] V. A. Kudryavtsev, Comput. Phys. Commun. 180, 339 (2009).
- [29] P. Antonioli, C. Ghetti, E. V. Korolkova, V. A. Kudryavtsev, and G. Sartorelli, Astropart. Phys. 7, 357 (1997).
- [30] A. Tang and G. Horton-Smith, V. A. Kudryavtsev, and A. Tonazzo, Phys. Rev. D 74, 053007 (2006).
- [31] M. Yamada, K. Miyano, H. Miyata, H. Takei, M. Mori, Y. Oyama *et al.*, Phys. Rev. D 44, 617 (1991).
- [32] E. Aprile et al., J. Phys. G: Nucl. Part. Phys. 40, 115201 (2013).
- [33] D. S. Akerib et al., Astropart. Phys. 125, 102480 (2021).
- [34] A. Gando et al. (KamLAND Collaboration), Phys. Rev. C 92, 055808 (2015).